Fracture toughness of reactive bonded Co–Mn and Cu–Mn contact layers after long-term aging

Yousef Alizad Farzin [a,*], Ilaria Ritucci [a], Belma Talic [a,b], Ragnar Kiebach [a], Henrik Lund Frandsen [a]

[a] Department of Energy Conversion and Storage, Technical University of Denmark, Lyngby Campus, 2800, Kgs. Lyngby, Denmark
[b] SINTEF Industry, Department of Sustainable Energy Technology, Postboks 124 Blindern, NO-0314, Oslo, Norway

ARTICLE INFO

ABSTRACT

Creating a tough bond for the electrical contact between metallic interconnects and ceramic solid oxide cells (SOC) in a stack is challenging due to restrictions on the assembly temperature. The reactive oxidation bonding in the formation of Co_2MnO_4 (CoMn) and $Cu_{1.3}Mn_{1.7}O_4$ (CuMn) spinel oxides from metallic precursors could provide a potential solution for achieving tough and well-conducting contact layers. These contact layers are deposited from metallic precursors onto CoCe-coated AISI441 substrates to achieve high toughness even after aging for 3000 h at typical operating temperatures for SOCs. The interface fracture energy of CoMn and CuMn contact layers was measured for as-sintered and aged samples by using a modified four-point bending test. After the fracture test, X-ray diffraction, electron microscopy, and energy-dispersive X-ray spectroscopy were used to determine phase evolution and possible reactions at the contact layer/interconnect interface. The results show that the interface fracture energy of sintered CoMn contact layer (6.1 J/m^2) decreased to 2.9 J/m^2 after aging at 850 °C for 3000 h while the fracture energy for CuMn increased from 6.4 J/m^2 to 19.7 J/m^2.

1. Introduction

Solid oxide cells (SOCs) are promising electrochemical devices that can be operated either in fuel cell mode (SOFC) for converting chemical energy to electricity or in electrolysis mode (SOEC) for producing H_2 and CO gas with high efficiency [1,2]. Operating SOCs at high temperatures promotes ionic and electronic conductivity and enhances the electrochemical reaction kinetics on the surface of the electrodes [3]. Because the voltage produced by a single cell is less than required for practical applications, it is necessary to provide an electrical connection between multiple cells via interconnects in a so-called stack.

The development of electrodes with improved electrochemical activity and thinner electrolytes enabled SOCs to be operated at the lower temperature range of 600–800 °C. This made it feasible to utilize metallic materials as the interconnect instead of more expensive ceramics [4–6]. Ferritic stainless steels (FSS) are commonly chosen as the interconnect material because of their excellent mechanical properties and ease of manufacture. Additionally, the compatibility of their coefficients of thermal expansion (CTE) with other stack components minimizes thermal stresses caused by temperature variations. However,

a high oxidation rate of FSS above 900 °C limits the stack assembly temperature.

Another challenge with FSS interconnects is the growth of Cr_2O_3 and $MnCr_2O_4$ layers on the steel surface, which increases the ohmic resistance of the stack [7]. Furthermore, these oxides are prone to volatilize into gaseous Cr(VI)-species that lead to Cr-poisoning of the oxygen electrode under an oxidizing atmosphere [8,9]. To mitigate these issues, protective coatings must be applied [10]. A thin (600 nm) metallic layer of Ce + Co deposited by physical vapor deposition (PVD) has been shown to be particularly promising as a protective coating material [11].

Contact layers (CL) are often used to ensure good electrical and physical contact between the SOC electrodes and the interconnect [13]. Ni-mesh or -foam is typically used as the contact layer for the fuel electrode side of the SOCs. These serve as a ductile layer that adheres well to both the interconnect and electrode materials [12,13]. The flexibility and ductility of Ni allow for adsorbing some of the stress that may arise from thermal gradients across the stack and different CTEs in the adjacent components.

On the oxygen side, the contact layer needs to have chemical and microstructural stability, high electrical conductivity, chemical

* Corresponding author.
E-mail address: yoafar@dtu.dk (Y.A. Farzin).

compatibility, and matching CTE with adjacent components. High sinterability during stack assembly is an additional requirement to achieve high toughness [14]. The many constraints for the oxygen electrode contact layer limit the number of candidates to i) precious metals such as Ag, Pt, Au, and Pd, ii) state-of-the-art electrode materials with perovskite structure, and iii) spinel oxides in the Mn–Co, Mn–Cu, and Ni–Fe systems.

The high electronic conductivity and oxidation resistance of precious metals make them a superior candidate for the oxygen electrode contact layer, but their use is practically limited due to the high cost. Perovskites with an ABO_3 structure have been widely developed as SOC electrodes, where the A-site is a lanthanide rare earth cation, and the B-site is a transition metal cation such as Co, Cu, Mn, Fe, or Ni [6,13]. Previous studies have focused on tailoring existing oxygen electrode materials to serve as contact layer material [15,16]. The perovskite contact layer is typically applied as ink with ceramic particles, deposited using blade coating, plasma spraying, wet powder spraying, or screen-printing [13, 17,18], and sintered during the stack assembly. The required temperature for the sintering of perovskites is in the range of 1050–1400 °C [14, 19,20]. However, the high oxidation rate of stainless steels and the use of glass-ceramic sealants limits the stack assembly temperature to below 900 °C. Consequently, the formation of a dense layer with desirable electrical and mechanical properties has been hindered by insufficient sintering of the contact layer. The pure perovskite contact layers are relatively weak, with fracture energies in the order of 1–2 J/m^2 [21].

A number of optimizations of perovskite-based CLs have been attempted, including improving powder size and using glass to improve the robustness [14,21]. However, adding glass to a perovskite oxide CL lowers the conductivity and enhances the potential for undesired chemical interactions at the CL/electrode and CL/interconnect interfaces [13].

Recently, it has been shown that spinel oxides, e.g. (Mn, Co, Fe, Ni, Cu)$_3$O$_4$, require lower sintering temperatures than perovskites and can be a third candidate as the CL material [13]. The improved densification during SOC stack assembly may provide higher interface adhesion at the electrode/interconnect interface. In addition, a high electrical conductivity, good ability to suppress chromia formation, and compatible CTE with the interconnect and electrode materials make spinel oxides promising candidates for the oxygen electrode contact layer [22,23].

The (Mn, Co)$_3$O$_4$ spinel oxide can slow down the oxidation rate of the interconnect and has high electrical conductivity (60 S cm^{-1} at 800 °C) and acceptable CTE (11.4–14.4 × 10^{-6} K^{-1} between 25 and 800 °C [24]) [13]. The (Cu, Mn)$_3$O$_4$ spinel oxide has higher electrical conductivity (225 S cm^{-1} at 750 °C) and is another material that could mitigate the issue of increasing SOC stack resistance with time [25].

Ritucci et al. [26] screen-printed Co + Mn and Cu + Mn metallic powders onto bare Crofer 22 APU and sintered at 800 °C to form the spinel oxides mentioned earlier in-situ oxidation. By applying the metal powders in a stoichiometric ratio, well-conducting spinels were formed over time by in-situ oxidation and interdiffusion. High toughnesses of 6.0 J/m^2 for the CoMn and 13.5 J/m^2 for the CuMn contact layers were achieved immediately after sintering at 800 °C [26]. After aging in the air for 250 h at 750 °C, the fracture energy dropped to 3.9 J/m^2 for the CoMn and 5.0 J/m^2 for the CuMn contact layer, respectively. The decrease in fracture energy after aging was attributed primarily to the oxidation of the uncoated steel substrates and the formation of a weak oxide scale.

In this work, the same contact layers are deposited onto CoCe coated AISI 441 interconnects to study the impact of a coating on fracture energy during aging. The phase evolution and microstructural change after in-situ densification from metallic powders are characterized, and the mechanical properties after aging for 250 and 3000 h at 750 and 850 °C are investigated. The chemical interaction at the interface of the applied contact layer with CoCe coated 441 ferritic stainless steel is studied by SEM and XRD. Moreover, the adherence of the oxide scale to the metallic substrate is measured to assess its impact on the assembly.

2. Experimental

The fracture energy of a Co–Mn and Cu–Mn contact layer on CoCe-coated AISI441 interconnect (Sandvik Materials) was measured using a special four-point bending fixture (FPB). In order to investigate the adhesion of the coating/oxide scale to the metallic substrate, a well-adhering glass-ceramic with high fracture energy was used as a "glue" between the layers [27,28].

The samples consisted of a layered structure where the adhering layer (contact layer or glass-ceramic) was sandwiched between a long strip of stainless steel on the top and two short strips on the bottom. Fig. 1 shows the sample geometry and the configuration of the particular FPB test. The bottom sandwich layer is discontinuous at the middle of the sample to generate a stress localization, where a crack will initiate when the sample is put under load. The preparation of the samples and the experimental method is described further in section 2.1 and 2.2, respectively.

2.1. Sample preparation

A slurry with the appropriate ratio of either Co, Cu, and Mn metal particles or glass powder was applied by screen-printing on the bottom (short) metallic substrates. The samples were assembled by sandwiching the screen-printed short metallic strip with the top long metallic strip, such that the contact layer/glass layer was in the center. The sandwiches were thereafter heat-treated in air, through which the reactive oxidative bonding took place, and the conductive spinel oxides formed.

The metallic substrate used for this study was AISI441 stainless steel (Cr = 17.5 wt%, Mn = 0.4 wt%, Si = 0.6 wt%, Nb = 0.4 wt%, Ti = 0.2 wt %, Ni = 0.1 wt%, Al <0.1 wt%, Fe = rest) with CoCe coating deposited by physical vapor deposition (PVD) at Sandvik Materials [29,30]. The metallic substrates were laser-cut to the desired dimensions (Fig. 1).

To prepare slurries with the targeted Co$_2$MnO$_4$ (CoMn) and Cu$_{1.3}$Mn$_{1.7}$O$_4$ (CuMn) compositions, Cu, Mn, and Co metal powders were mixed by planetary ball-milling (RETSCH-PM 400) using zirconia cups and balls. The mixtures of Mn (31.77 wt%) - Co (69.23 wt%) and Cu (47.16 wt%) - Mn (52.84 wt%) metal powders were used in order to achieve the desired stoichiometry of the spinel oxides. The measured particle size for Mn (American elements), Co (Alfa Aesar), and Cu (Alfa
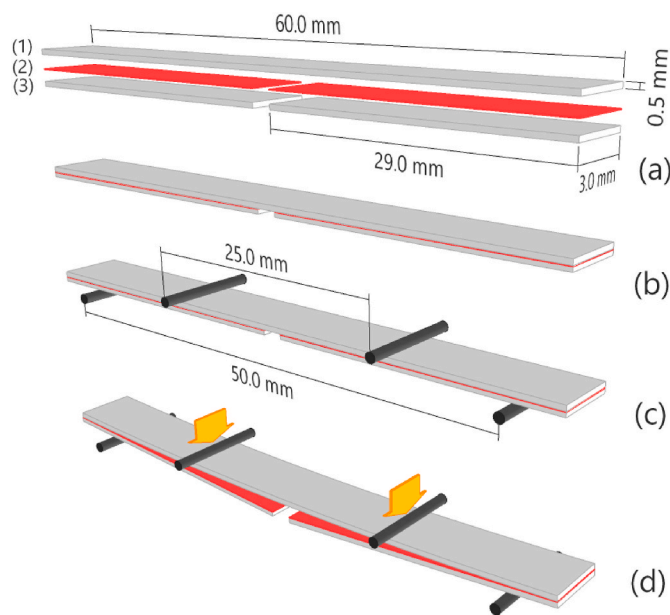

Fig. 1. The schematics of (a) sample components and geometry, (b) assembled sample, (c) configuration of four-point bending test, and (d) failure mechanism in the loaded sample.

Aesar) was about 2, 1.6, and 2 μm, respectively. BET analysis showed that the surface area for the Co, Cu, and Mn powders was 1.211, 0.376, and 0.390 m^2/g, respectively. Slurries for screen printing were prepared by mixing the metals powder with Dipropylenglycol (DPG), Poly-vinylpyrrolidone (PVP) K30, and K90 as the solvent and binders.

A previous study has shown that a Ba-free glass-ceramic has superior surface adhesion and good chemical compatibility with ferritic stainless steel [28]. Therefore, this glass-ceramic was used to study the adherence of the oxide scale by introducing it as a central layer in the above-described sandwich feature instead of the contact layer. The glass consisted of 46.4% SiO$_2$, 13% MgO, 14.3% CaO, 9.3% Na$_2$O, 8.3% Al$_2$O$_3$, 2.9% ZrO$_2$, and 5.8% B$_2$O$_3$ (all in wt.%) and was produced by melting the oxide powders in a platinum crucible at 1300 °C for 2 h followed by quenching in water. Then, 70 wt% of glass powder was mixed with 30 wt% of an organic paste consisting of solvent, binder, surfactant, and plasticizer to form a glass slurry. The thermo-mechanical properties and phase evolution of this glass have been studied previously [28].

As a means of simulating the assembly conditions inside a SOC stack, the samples were heat-treated under a load of 16.7 N/cm^2 at 800 °C in the air. The sintering process involved heat treatment up to 600 C with a 15 °C/h heating rate and a hold for 1 h to remove the solvent and binders. Afterward, the temperature was increased to 800 °C at 60 °C/h and held for 1 h to sinter the samples. Finally, cooling down to room temperature was done at the rate of 60 °C/h to moderate thermal stress at the contact layer/interconnect interface. The thickness of the green and sintered contact layers applied via the screen-printing technique was estimated at 95 ± 5 and 62 ± 2 μm, respectively.

Subsequently, the samples were exposed to air at 750 and 850 °C for 250 and 3000 h to investigate the aging effect on the contact layer's microstructure, phase composition, and mechanical properties. For the samples with a glass-ceramic layer, the coated substrate was aged for 250 h at 750 and 850 °C before applying the glass ceramic. After that, some of the samples were further aged for 2750 h (i.e., 3000 h total) at 750 and 850 °C. Before applying the glass, the pre-aging for 250 h was done to minimize the stainless steel and glass-ceramic interactions. The details of the naming and aging temperatures for the prepared samples are summarized in Table 1.

2.2. Characterization

The fracture energy was measured at room temperature with a four-point bending fixture built in-house at DTU Energy [31,32]. The fixture used for this study had a distance between inner and outer pins of 25 and 50 mm, respectively. The schematic of the pins' position is provided in Fig. 1. The load was applied under displacement control with a displacement rate of 0.01 mm s^{-1}. In order to obtain reproducible data

Table 1
The coding system for sintered and aged samples for 250 and 3000 h. Five samples were tested for each combination to ensure the reproducibility of data.

Contact layer	Sample name	Sintering + aging temperature (°C)	Aging duration (h)
Co$_2$MnO$_4$	#CoM	800 + (−)	–
	#CoM250h750	800 + 750	250
	#CoM250h850	800 + 850	250
	#CoM3kh750	800 + 750	3000
	#CoM3kh850	800 + 850	3000
Cu$_{1.3}$Mn$_{1.7}$O$_4$	#CuM	800 + (−)	–
	#CuM250h750	800 + 750	250
	#CuM250h850	800 + 850	250
	#CuM3kh750	800 + 750	3000
	#CuM3kh850	800 + 850	3000
Glass-ceramic	#G250h750	800 + 750	250
	#G250h850	800 + 850	250
	#G3kh750	800 + 750	3000
	#G3kh850	800 + 850	3000

for each measurement, five samples were tested for each combination. The load-displacement curves of prepared samples are shown in Fig. 3. The fracture energy is calculated based on the critical load in the load-displacement curve at the onset of interfacial cracking. The part of the strip in which the interfacial crack will grow is subjected to a constant moment (M$_b$) according to Eq. (1) [33]:

$$M_b = \frac{Pl}{2b} \tag{1}$$

P, b, l denote the applied force for initiating the crack, the sample width, and half the difference between the outer and inner spans. The steady-state energy release rate G$_{ss}$, here also referred to as fracture energy, can be calculated using the following formula

$$G_{ss} = \frac{M_b^2(1 - v_1^2)}{2E_1}\left(\frac{1}{I_1} - \frac{1}{I_c}\right) \tag{2}$$

where E$_1$ is Young's modulus, ν_1 is Poisson's ratio, and I$_1$ is the second moment of area of the through-going substrate of AISI441. I$_c$ is the combined second moment of area of the bottom strip and the spinel oxide layer. The indexes 1, 2, and 3 refer to the top strip, spinel oxide layer, and bottom strip, respectively (see Fig. 1). The second moments of areas are calculated as:

$$I_1 = \frac{h_1^3}{12} \tag{3}$$

where h$_1$ is the thickness of the substrate and I$_c$ is given by:

$$I_c = \frac{h_1^3}{3} + \kappa\frac{h_2^3}{3} + \mu\left(\frac{h_3^3}{3} + h_3^2 h_2 + h_2^2 h_3\right) - \frac{[h_1^2 - \kappa h_2^2 - \mu(h_3^2 + 2h_2 h_3)]^2}{4(h_1 + \kappa h_2 + \mu h_3)} \tag{4}$$

κ is the ratio between the stiffness of the substrate and the spinel oxide layer:

$$\kappa = \frac{E_2(1 - \nu_1^2)}{E_1(1 - \nu_2^2)} \tag{5}$$

and μ is the ratio between the stiffness of the stiffener and the substrate

$$\mu = \frac{E_3(1 - \nu_1^2)}{E_1(1 - \nu_3^2)} \tag{6}$$

Considering the fact that the substrate and stiffener are made from the same material, the Poisson's ratios (ν) are the same, $\nu_1 = \nu_3 = 0.3$ [34]. Moreover, the significant differences in the thickness of the spinel oxide layer with substrate and stiffener make the results practically insensitive to Poisson's ratio of the oxide layer.

The Young's modulus for AISI441 stainless steel is E$_1$ = E$_3$ = 220 GPa [35] and E$_2 \approx$ 190 GPa [36]. Similar to Poisson's ratio, the geometry of the prepared sample makes it insensitive to variations in Young's modulus of the applied layer, e.g., assuming that E$_2$ is double, then the energy release rate changes by 0.001%.

The phase formation and crystal structure were investigated by X-ray diffraction at room temperature in the 2θ range of 20–70 degrees using a Bruker D8 Advance diffractometer with CuK$_\alpha$ radiation (k = 1.5418 Å). After the four-point bending test, the microstructure of the fracture surface and the cross-section were examined with scanning electron microscopy (Zeiss-Merlin FE-SEM) to characterize the cracking path. In addition, an energy dispersive spectrometer (EDS) in map mode was used for composition analysis to determine various elemental distributions on the fracture surface.

3. Results

3.1. Fracture energy measurements

An overview of fracture energy values for the as-sintered and aged samples at 750 and 850 °C is shown in Fig. 2. It is worth mentioning that
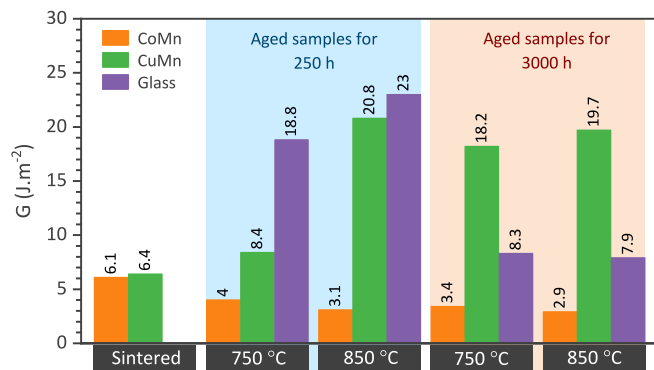
Fig. 2. The fracture energy (J/m^2) of sintered and aged samples at 750 and 850 °C for glass-ceramic, Co_2MnO_4 (CoMn), and $Cu_{1.3}Mn_{1.7}O_4$ (CuMn) spinel oxides according to the four-point bending test.

the thickness of the applied contact layer (62 ± 2 μm) is considerably thinner than the total thickness of the upper and lower substrate (1000 μm) in the sandwiched samples. For this reason, it can be assumed that the contact layer thickness did not have a significant influence when calculating the interface fracture energy. The calculated fracture energy values for the CoMn and CuMn contact layers are almost the same after sintering at 800 °C, i.e., 6.1 J/m^2 for #CoM and 6.4 J/m^2 for #CuM, respectively. Aging the samples at 750 and 850 °C leads to a different behavior after 250 and 3000 h. In the CoMn contact layer, aging temperatures and duration lead to a decrease in fracture energy, while the CuMn contact layer shows an improvement in fracture energy.

Fig. 3 shows the load-displacement curves for the prepared samples after sintering and aging for 250 and 3000 h. As seen in the figure, the load initially remains zero until the pins of the fixture make contact with the samples. After contact, the load increases linearly due to the linear elastic response of the integral sample. The fracture appears as a smooth or jagged plateau depending on the mechanical properties of the sample.

For the glass-ceramics (Fig. 3a), the load-displacement curves show that crack propagation proceeds steadily in a smooth plateau region. The highest fracture energy of 23.0 J/m^2 is obtained in the sample aged at 850 °C for 250 h. Considering that the coated steel was aged for 250 h prior to assembly with the glass-ceramic, any interaction at the interfaces is minimal and comparable among the samples investigated. After testing, this was confirmed by SEM analysis of the glass/steel interface, and corresponding SEM/EDS images are provided in the Supplementary Material (Fig. 1s).

Fig. 3b and c show the load-displacement curves for CoMn and CuMn contact layers. The slope of the load-displacement curve for CoMn oxide in all investigated samples is almost identical, while it depends on the crack initiation load in CuMn oxide. Both the fracture energy and stiffness of the CuMn contact layer improved after aging.

In spite of the different slopes in the elastic region, the CoMn and CuMn contact layers show similar behavior with linear load-displacement curves, where cracks initiate at a critical load after sufficient displacement. The load-displacement curves demonstrate a difference in crack growth behavior in these contact layers: either a smooth plateau region or a more jagged plateau (sawtooth) is visible. For the CoMn contact layer, the load for crack extension in a plateau region determines the G_{ss} for all the prepared samples. In particular, the average of the load measured during crack growth was used to calculate the fracture energy of the samples.

The samples with a CuMn contact layer show different behavior depending on the aging temperature. There is a jagged plateau in the load-displacement curve of the #CuM, #CuM250h750, and #CuM3kh750 samples. For these samples, the mean of the maximum load in the jagged plateau was considered for G_{ss} calculation because cracks in a real assembly would stop below this threshold. A mixed crack
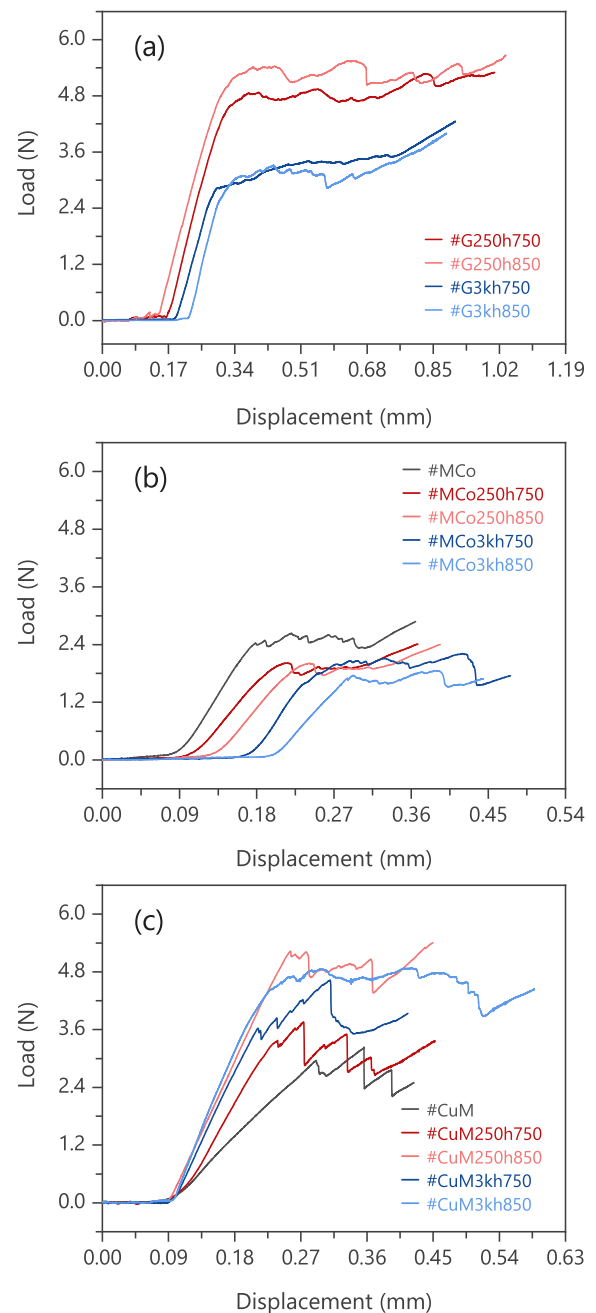

Fig. 3. The load-displacement curves for (a) samples with a glass-ceramic layer, (b) Co_2MnO_4 (CoMn), and (c) $Cu_{1.3}Mn_{1.7}O_4$ (CuMn) spinel oxide contact layers in as-sintered state and after aging at 750 and 850 °C for 250 and 3000 h. Note: the glass-ceramic layer was applied after aging of the CoCe coated AISI441 stainless steel, while the CoMn and CuMn contact layers were aged with the steel.

propagation mechanism was observed in the samples aged at 850 °C, and the average of the two plateau regions was taken.

In the third region of the load-displacement curve, the load began to increase again after long enough propagation of the crack in all applied layers. This occurs because the crack reached the inner loading bars, thus decreasing the driving force for further crack extension [37,38]. This region of the load-displacement curves was not taken into account.

3.2. X-ray diffraction patterns

Phase evolution in the sintered and aged samples was studied via

XRD after mechanical testing, and the obtained results were matched with Inorganic Crystal Structure Database (ICSD) cards. The XRD patterns for CoMn and CuMn oxide after sintering and aging at 750 and 850 °C are shown in Fig. 4. The XRD patterns were collected from the fracture surface to determine the phase composition in this area and study possible contact layer/substrate interface reactions.

3.2.1. CoM samples

The XRD pattern of #CoM, Fig. 4a, shows the formation of CoMn oxide with two structures: Co_2MnO_4 with a cubic (F d −3 m) space group and $CoMn_2O_4$ with a tetragonal (I 41/a m d) space group. In addition, Co_3O_4 (ICSD #96-900-5889) forms as a secondary phase in the sintered sample. After short-term aging for 250 h, the reaction of Co_3O_4 with tetragonal $(Co, Mn)_3O_4$ (ICSD #96-434-0938) leads to the formation of cubic $(Co, Mn)_3O_4$ (ICSD #99-900-4750) as seen in (Fig. 4a, #CoM250h750 and #CoM250850). The cubic $(Co, Mn)_3O_4$ was detected as the main phase in #CoM250h750 samples, while some Co_3O_4 was still present. Aging at 850 °C promotes the reaction towards cubic $(Co, Mn)_3O_4$ with the elimination of Co_3O_4 (Fig. 4a for the #CoM250h850).

The X-ray diffraction pattern for the long-term aged samples indicates good phase stability for the sample aged at 750 °C (#CoM3kh750). However, with aging at 850 °C, a few extra peaks are appearing (#CoM3kh850). According to the reference cards, the peaks could possibly belong to $CoMnO_3$ (ICSD #99-900-4769). This suggests the spinel oxide transformed partially to perovskite structure, thus changing the Co/Mn ratio in CoMn spinel oxide and shifting its main peak from 36 to 35.5 degrees. The inset image is provided for each data to distinguish the diffraction position for these phases.

3.2.2. CuMn samples

The X-ray diffraction of the sintered CuMn sample (#CuM) identified the CuO (ICSD #96-901-6058), Cu_2O (ICSD #96-900-5770), Mn_2O_3 (ICSD #96-151-4104), Mn_3O_4 (ICSD #96-101-1263), and $(Cu,Mn)_3O_4$ (ICSD #99-900-5219) phases after sintering at 800 °C for 3 h (Fig. 4b). The remaining simple oxides in different forms postpone the formation of CuMn oxide in sintered samples. After short-term aging for 250 h at 750 °C, the detected phases in the #CuM250h750 sample consist of (Cu, Mn)$_3O_4$ and CuO oxides, and no Mn oxide is detected. The phase evolution was almost complete after a short period of aging at 850 °C (#CuM250h850), where neither copper oxide nor other secondary phases were detected.

Aging the samples for 3000 h causes changes to the chemical composition in the CuMn contact layer. The inset image shows that the main peak for CuMn oxide shifts to a lower degree with the formation of a Cr-doped structure, and aging at higher temperature in #CuM250h850 drives a larger shift. The diffraction peak position could be interpreted as a variation of the chemical composition and lattice parameters for CuMn oxide, possibly due to the incorporation of Cr into the spinel oxide lattice. Accordingly, the matched reference cards show the $(Cu, Mn)_3O_4$ with different reference cards, ICSD #99-900-5218 and ICSD #99-900-5219 for #CuM250h750 and #CuM250h850 samples, respectively.

3.3. Microscopy and energy-dispersive spectroscopy

After the four-point bending test, the samples were only partially fractured to the inner set of pins (see Fig. 1). The samples were manually broken entirely apart to analyze the fractured surface. There are two contact layer/stainless steel interconnect interfaces in the assembled specimens in Fig. 1. In the following description, the interface near the long strip is called the top interface, and the one near the short strip is called the bottom interface.

Coating and oxide layer adherence.

Fig. 5 shows the fracture surface of the glass-ceramic layer (#G250h850). This is representative of the fracture surface for all investigated samples with the glass-ceramic layer. The SEM images reveal that the oxide scale was delaminated from the steel during sample failure for most of the sample. The oxide layer contains Cr, Ti, and Si with an atomic percent of 91%Cr–7%Si–2%Ti on a cation basis (analysis of oxygen is not trustworthy with EDS). The fact that the fracture took place at the oxide scale/stainless steel interface indicates that the adhesion between the glass-ceramic and the oxide scale is relatively strong, making it possible to study the mechanical properties of the oxide layer as it evolves during aging.

3.3.1. CoMn contact layer

SEM images of the fracture surface and a schematic of the fracture mechanism in the CoMn contact layer are shown in Fig. 6. Microscopy analysis showed that the fracture mechanism for the CoMn contact layer is independent of the aging condition. For this reason, only images for the #CoM250h850 sample are shown. Here, the crack propagates mainly at the contact layer/CoCe coating interface, and in a few spots, within the contact layer.

SEM image with higher magnification of the fracture surface of the top substrate (Fig. 6c) shows large, agglomerated particles in a network
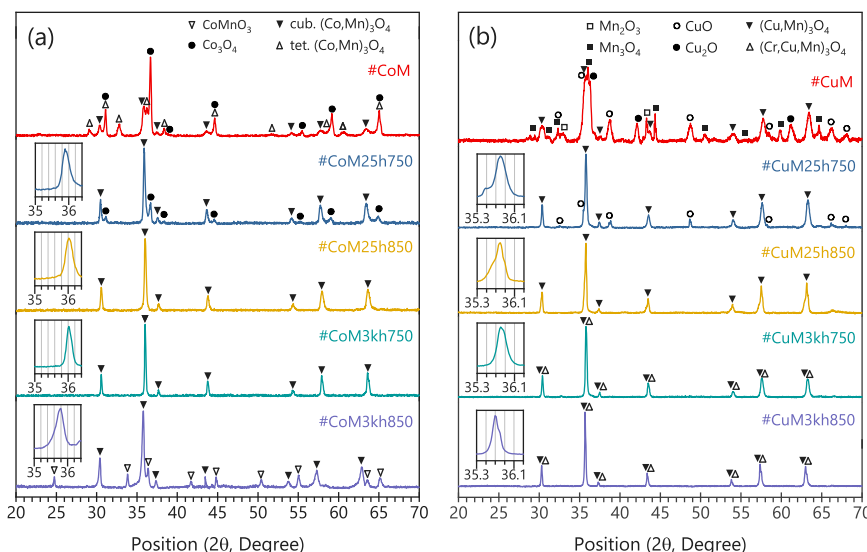

Fig. 4. X-ray diffraction patterns for (a) CoMn, and (b) CuMn contact layers, as-sintered and aged samples at 750 and 850 °C.
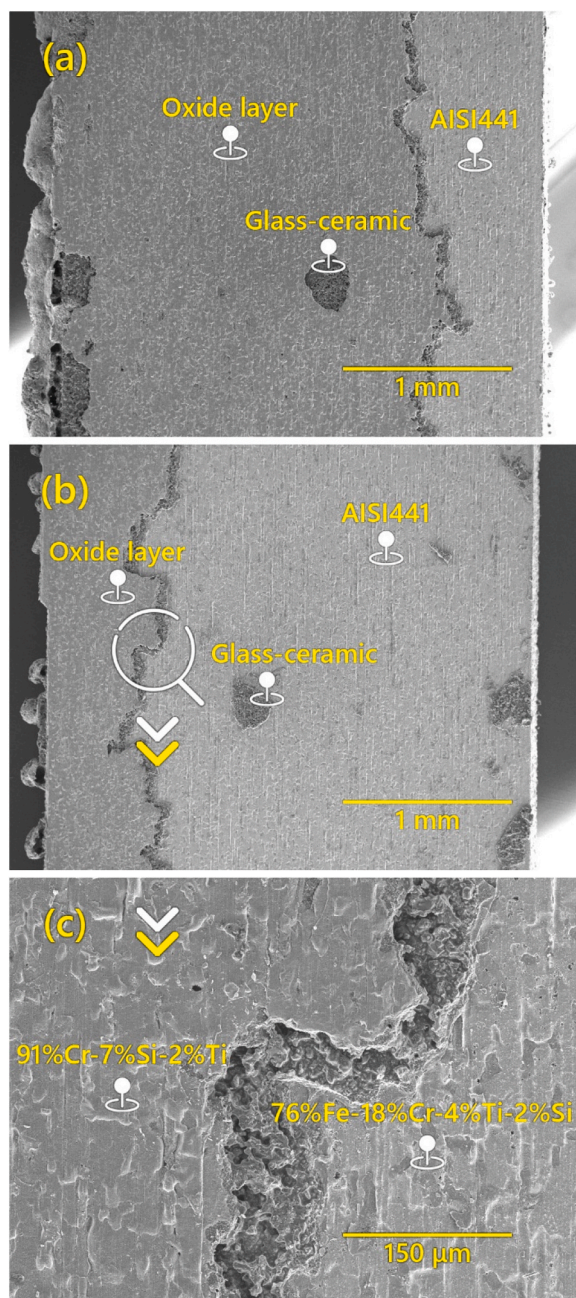
Fig. 5. SEM/EDS images of (a) top and (b) bottom failed interface in the sample with the glass-ceramic layer (#G250h850), (c) shows the bottom failed interface with higher magnification.

with smaller particles. The estimated mean size for an agglomerated island and the particles in the backbone network is approximately 2.5 μm and 0.4 μm, respectively. According to EDS point analysis, the chemical composition of the large particles corresponds to 34%Co–66% Mn oxide and that of the small particles to 42%Co–58%Mn oxide.

SEM image of the bottom substrate (Fig. 6d) shows a continuous CoCe coating layer on AISI441 stainless steel with a grain size of 2 μm. EDS analysis shows that the chemical composition equals 44%Co–44% Mn–10%Cr–6%Ti after aging for 250 h. As the CoCe coating is very thin and the EDS interaction volume several micrometers large, the Cr and Ti in this analysis likely originates from the oxide scale underneath the coating (see cross-sectional images in Fig. 7).

As a result of the fracture test, a few spots of the coating layer are delaminated, and the oxide scale exposes to the air. The oxide scale is

composed of 95%Cr–5%Ti (cation basis) according to EDS analysis and appears with a small grain size of 200 nm. Based on cross-sectional analysis (see Fig. 7b), this analysis most likely corresponds to a Cr_2O_3 scale with TiO_2 underneath due to the large EDS interaction volume.

SEM cross-section images of the CoMn contact layer for the aged samples are shown in Fig. 7. The images show the pathway of the crack propagation, the microstructure of the contact layers, and the oxide scale development after the short-term (250 h) and long-term (3000 h) aging. In addition, the chemical composition of the different phases at the contact layer/oxide scale interface is indicated in the figure using the EDS point analysis.

As seen in Fig. 7, the microstructure of the CoMn contact layer in all aged samples consists of large islands surrounded by smaller particles. Aging conditions were found to influence the dimensions of these features. The amount of small particles decreases with time, while the porosity in the layer increases (Fig. 7c and d). The porous areas could be potential pathways for crack propagation during fracture testing. As shown in Fig. 7, the CoMn contact layer failed through the porous region.

The composition of each layer can be difficult to determine from the cross-sectional SEM images since each layer is thin compared to the EDS interaction volume. Nevertheless, the EDS results for #CoM250h750 indicate some outward diffusion of Cr from the steel into the coating and contact layer during the aging process. The diffusion appears limited to less than a few micrometers into the coating/contact layer. The diffusion of Mn cations into the CoCe coating is another phenomenon observed for all investigated conditions. The bright layer close to the steel interface corresponds to the Ce layer of the protective CoCe coating.

EDS analysis of the sample aged at 850 °C (#CoM250h850) shows the formation of a thicker oxide scale on the stainless steel substrate compared to the sample aged at a lower temperature (Fig. 7b). According to the EDS analysis, this layer consists of mainly Cr cations, and its chemical composition is similar to the oxide scale in #CoM250h750. The Ti detected in this layer likely originates from the internal Ti-oxide precipitates underneath the oxide scale. After aging the samples at 850 °C, the Cr cations in the CoCe coating layer are more concentrated, resulting in a composition corresponding to 29%Co–23%Mn–48%Cr oxide. Nevertheless, the Cr diffusion only extends a few micrometers into the CoMn contact layer.

After 3000 h of aging, shown in Fig. 7c and d, the substrate/coating layer interface is not flat for both #CoM3kh750 and #CoM3kh850 samples, and the oxide scale thickness has increased to 2.7–3.8 μm. The bright dots corresponding to Ce could no longer be found after the long period of aging. The oxide scale consists mainly of Cr_2O_3 on the top with Ti-rich oxide precipitates underneath. The long-term aging causes the chromia scale to react with the CoCe coating. According to EDS analysis, the oxide scale/coating interface of the #CoM3kh850 sample has a higher fraction of Cr in the interdiffusion layer than the sample aged at 750 °C. Nonetheless, both samples showed no Cr detected within 4 μm of the oxide scale/coating interface, indicating good Cr retention capabilities of coating. The diffusion of Cr cations to the CoMn structure cause to migration of Mn cations out of the interdiffusion layer.

3.3.2. CuMn contact layer

Fig. 8 shows SEM images of the fracture surface and a schematic of the fracture mechanism in the #CuM250h850 contact layer. The fracture mechanism for the CuMn contact layer is different from the crack propagation in the CoMn contact layer. However, it shows a similar mechanism over the investigated conditions. Accordingly, only images corresponding to the short-term aged (250 h) sample at 850 °C are presented.

SEM images with higher magnification in Fig. 8c show a dense layer on top of the CuMn contact layer. Based on EDS results, the chemical composition in this area is 52%Mn–15%Cu–32%Cr. The fractography analysis with ImageJ software indicates that about 80% and 7% of the crack propagation has occurred through contact layer and oxide scale/
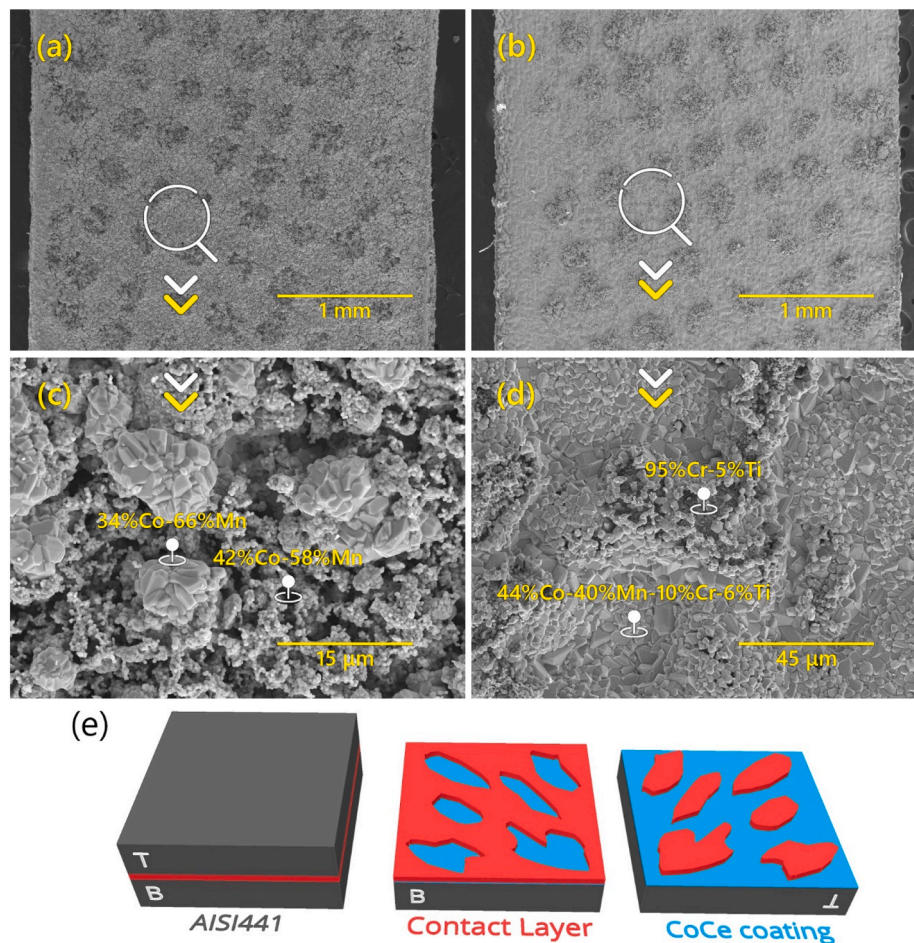
Fig. 6. The SEM images and schematic of fracture mechanism in Co_2MnO_4 (CoMn) contact layer after aging at 850 °C for 250 h (the blue area is the coating layer, and the red zone is the contact layer). Note: the T and B in the schematic of the fracture mechanism refer to the top and bottom strip in the sandwiched sample, respectively. (For interpretation of the references to color in this figure legend, the reader is referred to the Web version of this article.)

stainless steel substrate interfaces, respectively. The area where the crack has propagated at the oxide scale/stainless steel interface is shown with the dark gray color in Fig. 8e.

SEM cross-sectional images of the CuMn contact layer after aging for 250 and 3000 h are shown in Fig. 9. There is a noticeable difference in the density and homogeneity of the samples with CuMn oxide compared to CoMn oxide, and it is difficult to distinguish discrete particles in the CuMn microstructure. The SEM image for the #CuM250h750 sample illustrates that the crack propagated mainly at the contact layer/oxide scale interface.

SEM images of the sample aged at 850 °C (Fig. 9b) show higher porosity in the contact layer. The porosity is interconnected, forming a large hole perpendicular to the stainless steel substrate. Also, this is perpendicular to the crack growth direction and therefore cannot be considered as the crack growth pathway in the sample failure. The fracture mechanism in #CuM250h850 is different from the aged sample at 750 °C. In addition to the recognized path in #CuM250h750, the crack propagates within the contact layer and along with the CoCe coating layer/contact layer interface.

SEM images with higher magnification of the microstructure of short-term and long-term aged samples at 750 °C show a flake-like structure in the CuMn matrix. The EDS analysis of #CuM250h750 identifies these flakes as 70%Mn–30%Cu oxide, which is free of Cr cations compared to the base matrix has the chemical composition of 53%Mn–43%Cu–4%Cr oxide. This feature coarsens by increasing the aging period and finally covers the entire contact layer in #CuM3kh750. The chemical composition of the flakes in this sample is 58%Mn–41%

Cu–1%Cr, which still has a lower Cr concentration than the base matrix.

The EDS point results for the aged sample at 750 °C (#CuM250h750) indicate a thin layer formation near the steel surface. The chemical composition of this layer (30%Cr–27%Cu–40%Mn–3%Co) indicates outward diffusion of Cr into the contact layer while Cu diffuses towards the steel/coating interface (Fig. 9a). Thus, the CuMn contact layer displays a greater concentration of Cr cations than the corresponding sample with a CoMn contact layer. The Concentration of Cr species in CuMn oxide decreases with distance from the steel substrate and is below the detection limit at 4.2 μm. Similar to corresponding samples with the CoMn contact layer, a few Ti-rich oxides form near the stainless steel/oxide scale interface, and Ce is visible in the contact layer/coating.

The CoCe coating layer in #CuM250h850 shows that the bright dots corresponding to the Ce grains are disappeared with diffusing into the contact layer (Fig. 9b) and was not detected in samples aged for 3000 h. The EDS results show that aging at 850 °C causes the formation of a thicker chromia scale and enhanced diffusion of Cr into the contact layer. The contact layer composition adjacent to the oxide scale for this sample, i.e., #CuM250h850, is 55%Cr–23%Cu–20%Mn–2%Co.

SEM images for the long-term aged samples show the formation of a thick oxide scale (about 3 μm) on the stainless steel surface (Fig. 9c and d). The detected components in the oxide scale of #CuM3kh750 and #CuM3kh850 contain the Cr_2O_3 oxides with an obvious interface with the substrate. The Cr concentration in the adjacent CuMn layer is relatively high and decreases outward in the CuMn contact layer. Besides the high diffusion rate of Cr cations at high temperatures, the long-term aging of the sample provides suitable conditions to spread Cr species
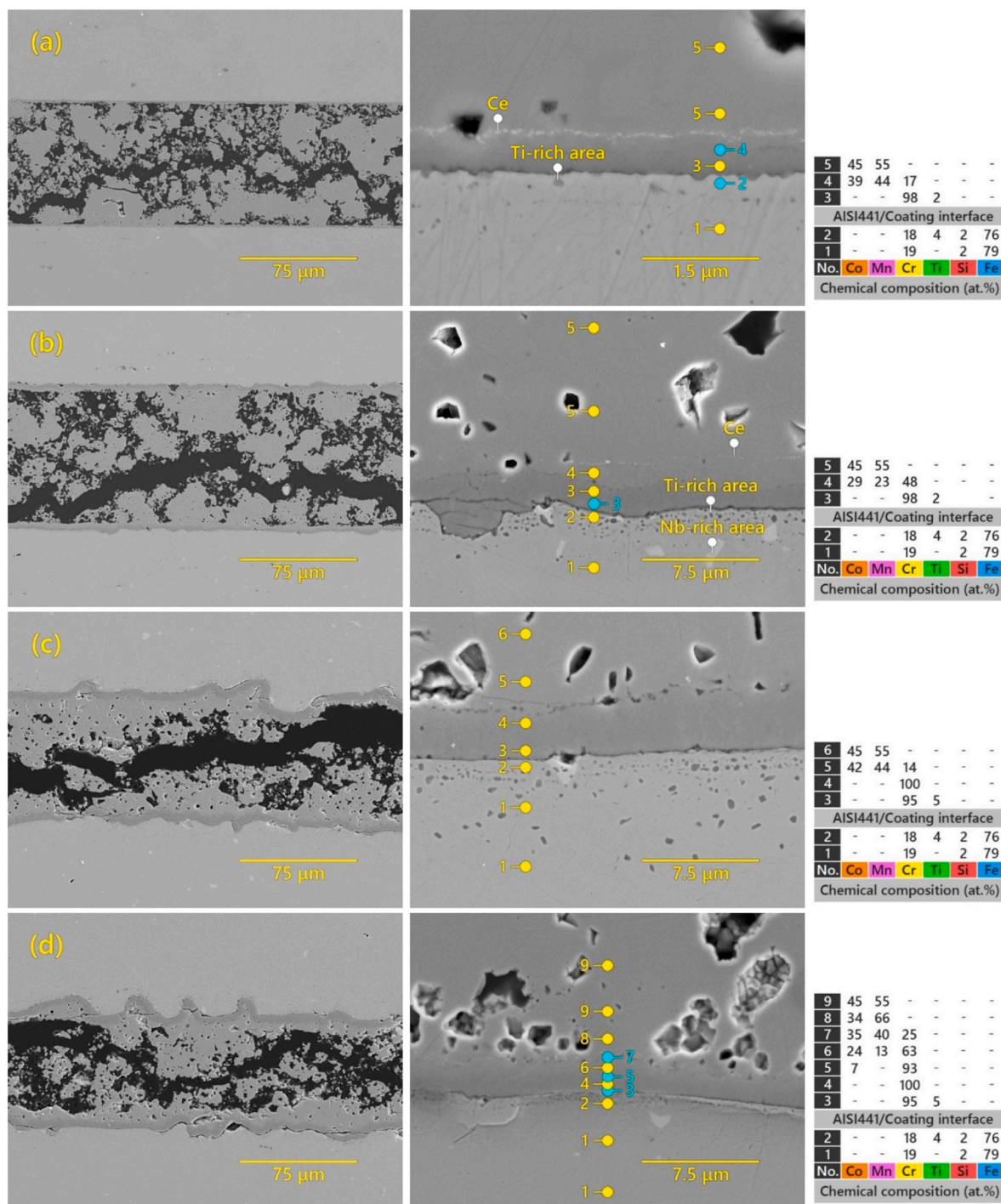
Fig. 7. Cross-section SEM images of failed interfaces in CoMn contact layer for the (a) samples aged at 750 °C for 250 h (#CoM250h750), (b) samples aged at 850 °C for 250 h (#CoM250h850), (c) samples aged at 750 °C for 3000 h (#CoM3kh750), and (d) samples aged at 850 °C for 3000 h (#CoM3kh850). The tables on the right-hand side show normalized concentrations (at. %) of cations based on EDS point analysis.

in the applied layer. Accordingly, the EDS results show Cr-doped CuMn oxide with the chemical composition of 35%Cu–59%Mn–6%Cr at the furthermost distance from the substrate.

4. Discussion

4.1. The oxide scale growth

The micrographs of the fracture surface in glass-ceramic bonded samples show good adhesion of glass-ceramic to the CoCe coated

AISI441 stainless steel (Fig. 5). Accordingly, the oxide scale peels off completely during FPB testing due to the solid applied layer and the excellent bonding of the glass-ceramic to the formed oxide scale. This means that the fracture energy for these samples is limited by the oxide scale/steel substrate interface toughness. In other words, the obtained fracture energy of 18.8 and 23.0 J/m^2 for the samples aged at 750 and 850 °C for 250 h is the intrinsic fracture energy of the oxide scale formed on CoCe coated AISI441 stainless steel.

The variation of fracture energy demonstrates significant influences of the mechanical properties to the period of the aging process. It
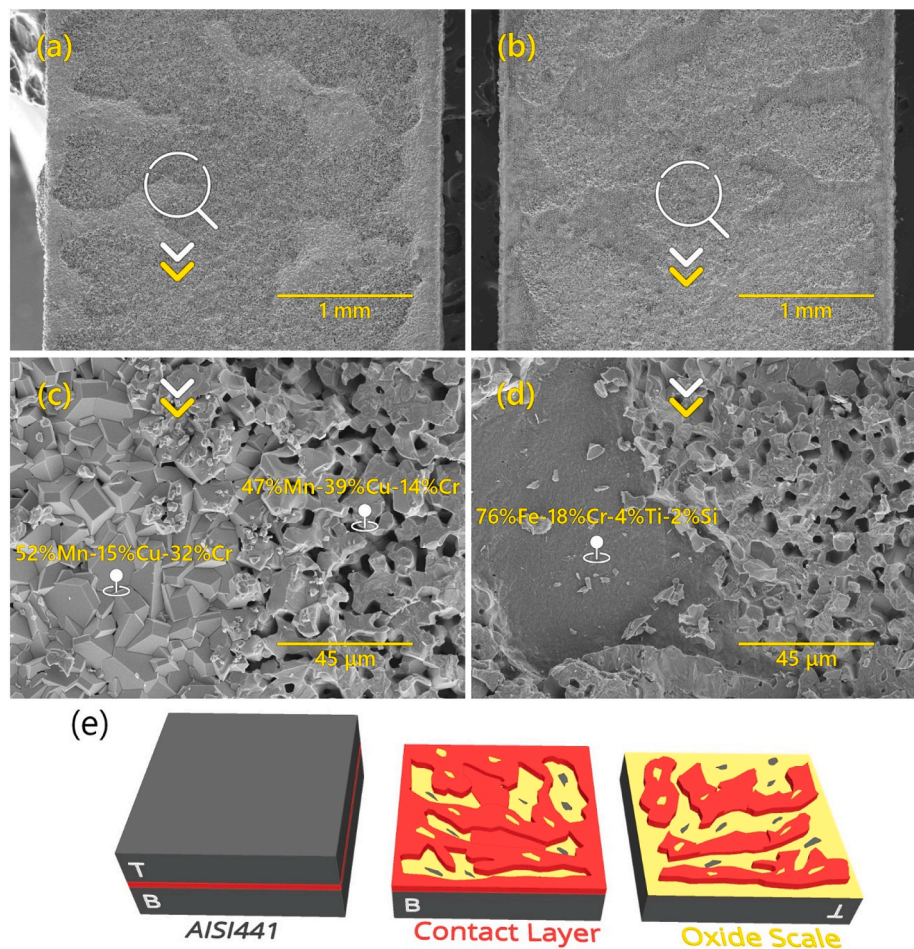
Fig. 8. SEM images and schematic of fracture mechanism in samples with $Cu_{1.3}Mn_{1.7}O_4$ (CuMn) spinel oxide contact layer after aging at 850 °C for 250 h (the yellow area is the oxide scale, and the red zone is the contact layer). Note: the T and B in the schematic of the fracture mechanism refer to the top and bottom strip in the sandwiched sample, respectively. (For interpretation of the references to color in this figure legend, the reader is referred to the Web version of this article.)

decreased from 18.8 to 8.3 J/m^2 in #G3khh750 and 23 to 7.9 J/m^2 in #G3kh850. The decrease in fracture energy is mainly due to the growth of the oxide scale after aging for 3000 h. The oxide scale thickness is approximately 2.8 μm for #G3khh750 and 4.0 μm for #G3kh850, respectively. The long-term aged sample at 850 °C (#G3kh850) has the weakest mechanical properties among the prepared samples with the glass-ceramic layer (fracture energy of 7.9 J/m^2). Since the glass-ceramic layer does not take part in a chemical reaction with oxide scale (Fig. 1s), we believe that the cation interdiffusion in the glass-ceramic layer/oxide scale interface has not influenced the fracture energies of sandwiched glass-ceramic samples. This is consistent with the hypothesis of the decrease of fracture energy due to increased corrosion scale thickness of the uncoated steel in Ref. [26]. In the following section, the obtained fracture energies are compared with corresponding values in the CoMn and CuMn contact layers to study their robustness.

4.2. The fracture mechanism in the contact layers

The load-displacement curves for the CoMn and CuMn contact layers show two different crack propagation behaviors. The first is crack propagation in a plateau region called crack creeping [39]. This behavior in sample failure is also known as stable crack propagation [40]. The FPB results and fracture images of investigated samples reveal that stable crack propagation happens when the crack propagates through the same phase and microstructure. This microstructure could be either a porous or solid layer. Because the measurement was conducted in displacement control mode, the crack propagates along with a

connected porosity under nearly the same load in the case of porous microstructure.

In the second case, the crack extension occurs through a dense layer with a homogenous phase, and stress concentration in the crack tip is the dominant mechanism in the sample failure. It is found that chemical and structural stability are the main requirements in generating a dense contact layer. The single-phase contact layer with a uniform microstructure provides the same fracture energy all over the contact layer, leading to crack propagation parallel to the interfaces. Consequently, the samples gradually failed with the crack growth through the contact layer or at the contact layer/coating interface. The crack creeping mechanism has been observed for the prepared sample with CoMn oxide, glass-ceramic layer, and aged CuMn oxide for 3000 h.

The as-sintered and the aged CuMn contact layer at 750 °C showed a few load drops in the load-displacement curve during crack propagation, which indicates a different fracture mechanism in these samples (Fig. 3b). This kind of behavior classifies as a bursting type of crack propagation, where the crack grows during the load drop [37]. In general, hindering the crack propagation by the secondary phase is believed to be the main reason for this phenomenon. The secondary phases could be a solid grain or ductile particle, where further crack extension requires a higher load. Consequently, the secondary phases could fail by stress concentration in the crack tip at the higher loads. The failures in the secondary phases coincide with the crack extension and load drop in the load-displacement curve. This behavior is observed in a CuM contact layer with CuO as a ductile phase (#CuM) and aged ones at 750 °C with a solid contact layer and robust interfaces (#CuM250h750 and
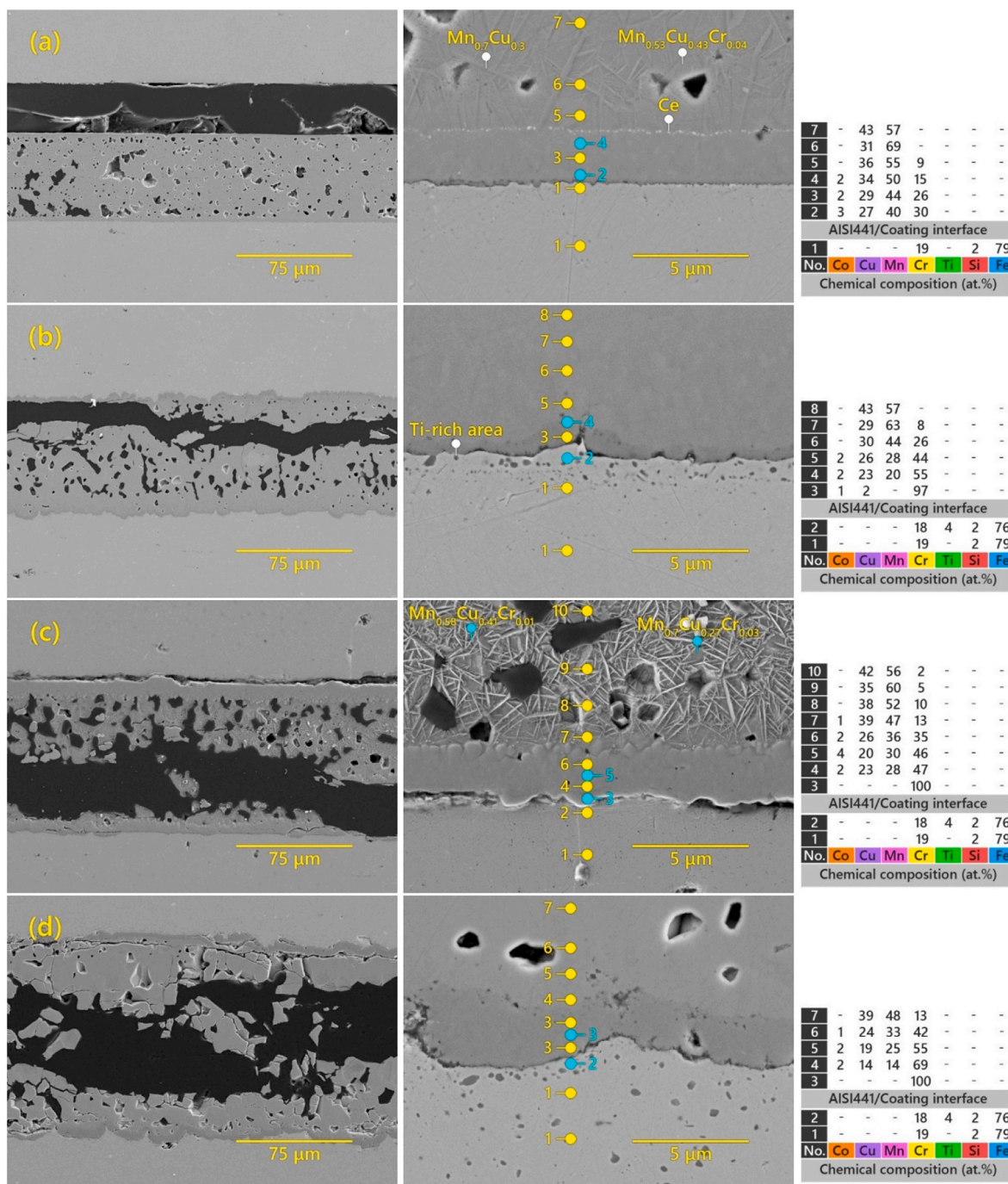
Panel (a) — Chemical composition (at.%)

No.	Co	Cu	Mn	Cr	Ti	Si	Fe
7	-	43	57	-	-	-	-
6	-	31	69	-	-	-	-
5	-	36	55	9	-	-	-
4	2	34	50	15	-	-	-
3	2	29	44	26	-	-	-
2	3	27	40	30	-	-	-
AISI441/Coating interface							
1	-	-	-	19	-	2	79

Panel (b) — Chemical composition (at.%)

No.	Co	Cu	Mn	Cr	Ti	Si	Fe
8	-	43	57	-	-	-	-
7	-	29	63	8	-	-	-
6	-	30	44	26	-	-	-
5	2	26	28	44	-	-	-
4	2	23	20	55	-	-	-
3	1	2	-	97	-	-	-
AISI441/Coating interface							
2	-	-	-	18	4	2	76
1	-	-	-	19	-	2	79

Panel (c) — Chemical composition (at.%)

No.	Co	Cu	Mn	Cr	Ti	Si	Fe
10	-	42	56	2	-	-	-
9	-	35	60	5	-	-	-
8	-	38	52	10	-	-	-
7	1	39	47	13	-	-	-
6	2	26	36	35	-	-	-
5	4	20	30	46	-	-	-
4	2	23	28	47	-	-	-
3	-	-	-	100	-	-	-
AISI441/Coating interface							
2	-	-	-	18	4	2	76
1	-	-	-	19	-	2	79

Panel (d) — Chemical composition (at.%)

No.	Co	Cu	Mn	Cr	Ti	Si	Fe
7	-	39	48	13	-	-	-
6	1	24	33	42	-	-	-
5	2	19	25	55	-	-	-
4	2	14	14	69	-	-	-
3	-	-	-	100	-	-	-
AISI441/Coating interface							
2	-	-	-	18	4	2	76
1	-	-	-	19	-	2	79

Labels in images: $Mn_{0.7}Cu_{0.3}$, $Mn_{0.53}Cu_{0.43}Cr_{0.04}$, Ce (panel a); Ti-rich area (panel b); $Mn_{0.58}Cu_{0.41}Cr_{0.01}$, $Mn_{0.7}Cu_{0.27}Cr_{0.03}$ (panel c).

Fig. 9. Cross-sectional SEM images of the failed interface in CuMn contact layer for the (a) samples aged at 750 °C for 250 h (#CuM250h750), (b) samples aged at 850 °C for 250 h (#CuM250h850), (c) samples aged at 750 °C for 3000 h (#CuM3kh750), and (d) samples aged at 850 °C for 3000 h (#CuM3kh850). The tables on the right-hand side show normalized concentrations (at. %) of cations based on EDS point analysis.

#CuM3kh750).

4.3. CuMn contact layer

The load-displacement curves of #CoM and #CuM samples exhibit almost the same fracture energy after sintering at 800 °C (6.1 and 6.4 J/m^2, respectively). However, the aging of the samples at 750 and 850 °C affected the mechanical properties in these contact layers differently. The fracture energy for the CuMn contact layer effectively improves during the aging process. The load-displacement curves of #CuM250h850 samples show high fracture energy of 20.8 J/m^2, which is significantly higher than reported values for the LSM (1–1.1 J/m^2),

LSC (0.7–1 J/m^2), and LNF (1.4 J/m^2) contact layer materials [41].

Based on microstructural images and X-ray diffraction patterns for aged CuMn oxide, the enhancement of mechanical properties in #CuM250h750 and #CuM250h850 could originate from two factors in parallel. The first one is related to the intrinsic fracture toughness of the contact layer, and the second is the chemical interaction in the contact layer/oxide scale interface. The intrinsic fracture toughness of the contact layer mainly originates from the phase evolution and final phase in the CuMn layer. The X-ray diffraction for the #CuM sample (Fig. 4b) shows that the (Cu, Mn)$_3$O$_4$ forms during the first heat treatment at 800 °C. However, the CuO is detected in the structure of the sintered sample and remains after aging for 250 h in #CuM250h750. The remaining CuO

could be due to the high sinterability of CuMn oxide to create a dense layer to hinder the diffusion of oxygen to beneath layers. On the other hand, copper oxide could act as a sintering aid to further improve the contact layer density. Whereas the cross-section SEM images in Fig. 7 illustrates high microstructural density in #CuM250h750 and #CuM250h850. The formation of a solid layer could also reason for the bursting crack propagation mechanism in the CuM samples.

The second explanation for the enhancement of fracture energy in the aged CuMn layer could be the chemical reaction of Cu cations with Cr species in the oxide scale. According to the point-EDS results in the corresponding interface (Fig. 9), Cu cations diffused inward and Cr species diffused outward to form an intermediate layer containing Co, Cu, Mn, and Cr cations. The chemical composition of the intermediate layer evolves with aging temperature and period, as the Cr concentration increases from 26 at.% in #CuM250h750 to 69 at.% in #CuM3kh850. It means that the diffusion rate of Cr species to CuMn structure is much higher than Cu and Mn cations to the chromia layer. The interdiffusion of Cr and Cu cations during aging effectively forms a chemically bonded interface, likely enhancing the interfacial adhesion. In other words, the chemical interaction at the contact layer/oxide scale interface ensures high fracture energy during aging, whereas the growth of the oxide scale causes weakening of mechanical properties. The effectiveness of chemical bonding is evident by comparing the obtained results for the glass-ceramic and CuMn contact layers. In contrast to the glass-ceramic, in which the G_{ss} decreases significantly after aging for 3000 h, the load-displacement curves for #CuM3kh750 and #CuM3kh850 show high fracture energy 18.2 and 19.7 J/m^2, respectively.

Finally, a solid structure with uniform microstructure and well-bonded interfaces could enhance physical bonding at high temperatures. As a result, the contact layer's detachment would not affect the electrical connection in a long-term operational period.

4.4. CoMn contact layer

The as-sintered CoMn contact layer (#CoM) shows fracture energy of 6.1 J/m^2, similar to the as-sintered #CuM. However, aging the samples weakens the fracture energy in the CoMn contact layer. For example, the calculated G_{ss} for #CoM3kh850 decreased to 2.9 J/m^2. It is found that three factors are responsible for determining the mechanical properties of the CoMn: 1) the formation of a porous microstructure, 2) the formation of two different CoMn oxides (cubic and tetragonal), and 3) limited chemical interaction at the contact layer/oxide scale interface.

The microstructural evolution of CoMn spinel oxide shows the formation of a network between small particles after sintering at 800 °C. These small particles grow and form bigger agglomerates after aging at high temperatures. Nevertheless, the microstructure remains porous after 3000 h of aging (Fig. 7). This is probably the most significant explanation for the low fracture energy in the CoMn contact layer.

The point EDS spectra identified the small grains having a high cobalt and oxygen concentration; these are the oxidized Co precursor during the sintering process (Fig. 7a). Similarly, the X-ray diffraction pattern for the #CoM sample (Fig. 4a) shows Co$_3$O$_4$ (ICSD #96-900-5889) as an intermediate phase in the formation of CoMn spinel oxide. The quantitative analysis shows that cobalt oxide covers about 25% of identified phases in the sintered sample.

After 250 h of aging at 750 and 850 °C (#CoM250h750 and #CoM250h850), the Co$_3$O$_4$ reacts with tetragonal (Co, Mn)$_3$O$_4$ and forms cubic (Co, Mn)$_3$O$_4$. The formation of the final CoMn phase improves the density of the contact layer, and fewer small particles are observed in SEM images (Fig. 7). Meanwhile, the formation of aggregated particles induces a large porosity to the microstructure and makes it highly susceptible to the applied load in the FPB test. The microscopy images illustrate that the CoMn contact layer mainly failed in the porous region.

Moreover, the formation of CoMn oxide with two crystal structures

of cubic (Co, Mn)$_3$O$_4$ (ICSD #99-900-4592) and tetragonal (Co, Mn)$_3$O$_4$ (ICSD #96-434-0938) is another limitation to form a solid layer in this contact layer. It is reported that Mn^{2+} and Mn^{3+}/Mn^{4+} occupy the tetrahedral and octahedral in the CoMn spinel structure, respectively [42]. The main reason for the existence of cubic and tetragonal (Co, Mn)$_3$O$_4$ at the final composition is that the Mn ions have three oxidation states and consequently prefer to occupy different lattice sites [43]. Accordingly, the presence of multivalence Mn ions in various crystal sites causes a high possibility of phase transformation in CoMn oxide at different temperatures and oxygen partial pressure. As a result, phase transition coincides with varying the unit cell volume and reasons micro-crack in adjacent grain boundaries with different compositions. The XRD pattern in Fig. 4a shows a slight shift to a higher degree for #CoM250h850 due to a change in the lattice constant. According to Bragg's law, the lattice parameter in #CoM250h750 and #CoM250h850 are 8.29 and 8.26 Å, respectively.

$$\lambda = 2d\sin\theta \tag{7}$$

$$\frac{1}{d2} = \frac{h^2 + k^2 + l^2}{a^2} \tag{8}$$

where λ is the wavelength, a is the lattice constant, and hkl are the corresponding Miller indices. However, we believe that phase transition has a minor effect on the dwindling of fracture energy compared to the deleterious effect of forming a porous structure in the CoMn contact layer.

The limited reaction between the CoMn contact layer and the oxide scale is another limitation in achieving good adherence at the contact layer/oxide scale interface. The EDS results indicated that Cr diffusion to the CoMn contact layer is highly suppressed compared to the CuMn contact layer. The thickness of Cr-doped CoMn oxide after aging at 850 °C for 3000 h is estimated at 3.4 μm (Fig. 7d), which is significantly less than the Cr diffused distance in #CuM3kh850 (21.2 μm). Indeed, the CoMn oxide has been shown to be an excellent barrier against the oxidation of stainless steel substrates and suppressing the evaporation of Cr that can poison oxygen electrodes [44].

The deteriorating effect of aging at the SOC operating temperature makes it difficult to obtain a robust contact layer with CoMn precursors. Despite this, the fracture energy achieved after 3000 h of aging (3.4 J/m^2 for #CoM3kh750 and 2.9 J/m^2 for #CoM3kh850) is still higher than values reported for state-of-the-art contact layers such as LSM, LSC, and LNF [21,26,41].

5. Conclusion

Co$_2$MnO$_4$ (CoMn) and Cu$_{1.3}$Mn$_{1.7}$O$_4$ (CuMn) contact layers with superior mechanical properties were successfully developed through in-situ reaction sintering. The four-point bending experiment indicates similar fracture energy of 6.1 and 6.4 J/m^2 in as-sintered CoMn and CuMn contact layers. This is well above state-of-the-art perovskite contact layers with an interface fracture energy of 1–2 J/m^2. The fracture energy of these contact layers was influenced differently by the aging temperature and period. Accordingly, the fracture energy for CoMn oxide decreased to 2.9 J/m^2 while it improved to 19.7 J/m^2 for CuMn oxide after aging at 850 °C for 3000 h.

The high fracture energy in the CuMn oxide originates from the high density of the sintered layer and a good chemical bonding at the contact layer/oxide scale interface. The presence of CuO acts as a sintering aid and the chemical reactivity of Cu cations with Cr species from the oxide scale are beneficial for forming a tough contact layer. However, there is a concern regarding the interdiffusion of Cr and Cu in the oxide scale and contact layer since this could lead to Cr poisoning of the oxygen electrode. In contrast, the development of porous microstructure and limited chemical reaction in the contact layer/oxide scale interface are reasons for low fracture energy in the CoMn contact layer.

According to obtained results, it can be concluded that applying the oxidation protective CoCe layer along with using Cu, Co, and Mn metallic powders is successful in the optimization of contact layer properties. The solid contact layer provides a robust physical contact to maintain a high electronic conductivity and ensure stable long-term performance.

Declaration of competing interest

The authors declare that they have no known competing financial interests or personal relationships that could have appeared to influence the work reported in this paper.

Acknowledgment

Appendix A. Supplementary data

Supplementary data to this article can be found online at https://doi.org/10.1016/j.ceramint.2022.04.050.

References

[1] Y.A. Farzin, A. Babaei, T.L. Skafte, E. Stamate, A. Ataie, S.H. Jensen, Low-temperature preparation and investigation of electrochemical properties of SFM/CGO composite electrode, Solid State Ionics 356 (2020) 115435, https://doi.org/10.1016/j.ssi.2020.115435.

[2] Y. Alizad Farzin, A. Babaei, T. Løye Skafte, E. Stamate, A. Ataie, S.H. Jensen, Development of an SFMM/CGO composite electrode with stable electrochemical performance at different oxygen partial pressures, Int. J. Hydrogen Energy 47 (2022) 7915–7931, https://doi.org/10.1016/J.IJHYDENE.2021.12.104.

[3] L. Zhang, Q. Zhou, Q. He, T. He, Double-perovskites A2FeMoO6−δ (A═Ca, Sr, Ba) as anodes for solid oxide fuel cells, J. Power Sources 195 (2010) 6356–6366, https://doi.org/10.1016/j.jpowsour.2010.04.021.

[4] E.D. Wachsman, K.T. Lee, Lowering the temperature of solid oxide fuel cells, Science (80-) 334 (2011) 935–939, https://doi.org/10.1126/science.1204090.

[5] S.J. Geng, J.H. Zhu, Z.G. Lu, Evaluation of Haynes 242 alloy as SOFC interconnect material, Solid State Ionics 177 (2006) 559–568, https://doi.org/10.1016/j.ssi.2005.12.004.

[6] N. Mahato, A. Banerjee, A. Gupta, S. Omar, K. Balani, Progress in material selection for solid oxide fuel cell technology: a review, Prog. Mater. Sci. 72 (2015) 141–337, https://doi.org/10.1016/j.pmatsci.2015.01.001.

[7] B. Talic, S. Molin, K. Wiik, P.V. Hendriksen, H.L. Lein, Comparison of iron and copper doped manganese cobalt spinel oxides as protective coatings for solid oxide fuel cell interconnects, J. Power Sources 372 (2017) 145–156, https://doi.org/10.1016/j.jpowsour.2017.10.060.

[8] H. Falk-Windisch, J.E. Svensson, J. Froitzheim, The effect of temperature on chromium vaporization and oxide scale growth on interconnect steels for Solid Oxide Fuel Cells, J. Power Sources 287 (2015) 25–35, https://doi.org/10.1016/j.jpowsour.2015.04.040.

[9] C. Key, J. Eziashi, J. Froitzheim, R. Amendola, R. Smith, P. Gannon, Methods to quantify reactive chromium vaporization from solid oxide fuel cell interconnects, J. Electrochem. Soc. 161 (2014) C373–C381, https://doi.org/10.1149/2.0041409jes.

[10] F. Cheng, J. Sun, Fabrication of a double-layered Co-Mn-O spinel coating on stainless steel via the double glow plasma alloying process and preoxidation treatment as SOFC interconnect, Int. J. Hydrogen Energy 44 (2019) 18415–18424, https://doi.org/10.1016/j.ijhydene.2019.05.060.

[11] M. Bianco, J. Tallgren, J.E. Hong, S. Yang, O. Himanen, J. Mikkola, J. Van herle, R. Steinberger-Wilckens, Ex-situ experimental benchmarking of solid oxide fuel cell metal interconnects, J. Power Sources 437 (2019) 226900, https://doi.org/10.1016/J.JPOWSOUR.2019.226900.

[12] K.H. Tan, H.A. Rahman, H. Taib, Coating layer and influence of transition metal for ferritic stainless steel interconnector solid oxide fuel cell: a review, Int. J. Hydrogen Energy 44 (2019) 30591–30605, https://doi.org/10.1016/j.ijhydene.2019.06.155.

[13] J.H. Zhu, H. Ghezel-Ayagh, Cathode-side electrical contact and contact materials for solid oxide fuel cell stacking: a review, Int. J. Hydrogen Energy 42 (2017) 24278–24300, https://doi.org/10.1016/j.ijhydene.2017.08.005.

[14] M. Shen, P. Zhang, Progress and challenges of cathode contact layer for solid oxide fuel cell, Int. J. Hydrogen Energy 45 (2020) 33876–33894, https://doi.org/10.1016/j.ijhydene.2020.09.147.

[15] Z. Lu, G. Xia, J.D. Templeton, X. Li, Z. Nie, Z. Yang, J.W. Stevenson, Development of Ni1-xCoxO as the cathode/interconnect contact for solid oxide fuel cells, Electrochem. Commun. 13 (2011) 642–645, https://doi.org/10.1016/j.elecom.2011.03.034.

[16] X. Montero, F. Tietz, D. Stöver, M. Cassir, I. Villarreal, Comparative study of perovskites as cathode contact materials between an La0.8Sr0.2FeO3 cathode and a Crofer22APU interconnect in solid oxide fuel cells, J. Power Sources 188 (2009) 148–155, https://doi.org/10.1016/j.jpowsour.2008.11.083.

[17] M.J. Tsai, C.L. Chu, S. Lee, La0.6Sr0.4Co0.2Fe0.8O3 protective coatings for solid oxide fuel cell interconnect deposited by screen printing, J. Alloys Compd. 489 (2010) 576–581, https://doi.org/10.1016/j.jallcom.2009.09.114.

[18] Z. Xie, Q. Zhu, L. Fang, Flexible contact layer between cathode and interconnect of SOFC, ECS Trans. 25 (2019) 2825–2827, https://doi.org/10.1149/1.3205845.

[19] R.K. Lenka, P.K. Patro, J. Sharma, T. Mahata, P.K. Sinha, Evaluation of La0.75Sr0.25Cr0.5Mn0.5O3 protective coating on ferritic stainless steel interconnect for SOFC application, Int. J. Hydrogen Energy 41 (2016) 20365–20372, https://doi.org/10.1016/j.ijhydene.2016.08.143.

[20] B.K. Park, D.W. Kim, R.H. Song, S.B. Lee, T.H. Lim, S.J. Park, C.O. Park, J.W. Lee, Design of a dual-layer ceramic interconnect based on perovskite oxides for segmented-in-series solid oxide fuel cells, J. Power Sources 300 (2015) 318–324, https://doi.org/10.1016/j.jpowsour.2015.09.082.

[21] M.C. Tucker, L.C. Dejonghe, V. García-Negrón, R. Trejo, E. Lara-Curzio, Mechanical and electrochemical performance of composite cathode contact materials for solid oxide fuel cells, J. Power Sources 239 (2013) 315–320, https://doi.org/10.1016/j.jpowsour.2013.03.130.

[22] C. Jia, Y. Wang, S. Molin, Y. Zhang, M. Chen, M. Han, High temperature oxidation behavior of SUS430 SOFC interconnects with Mn-Co spinel coating in air, J. Alloys Compd. 787 (2019) 1327–1335, https://doi.org/10.1016/j.jallcom.2019.01.015.

[23] Y. Shao, P.Y. Guo, H. Sun, T.C. Zhou, J.T. Ding, K.X. Xu, Y.X. Wang, Y.X. Guo, D.P. Wang, X.H. Hou, Structure and properties of composite Ni–Co–Mn coatings on metal interconnects by electrodeposition, J. Alloys Compd. 811 (2019), https://doi.org/10.1016/j.jallcom.2019.152006.

[24] B. Talic, P.V. Hendriksen, K. Wiik, H.L. Lein, Thermal expansion and electrical conductivity of Fe and Cu doped MnCo2O4 spinel, Solid State Ionics 326 (2018) 90–99, https://doi.org/10.1016/j.ssi.2018.09.018.

[25] A. Petric, H. Ling, Electrical conductivity and thermal expansion of spinels at elevated temperatures, J. Am. Ceram. Soc. 90 (2007) 1515–1520, https://doi.org/10.1111/j.1551-2916.2007.01522.x.

[26] I. Ritucci, B. Talic, R. Kiebach, H.L. Frandsen, High toughness well conducting contact layers for solid oxide cell stacks by reactive oxidative bonding, J. Eur. Ceram. Soc. 41 (2021) 2699–2708, https://doi.org/10.1016/j.jeurceramsoc.2020.11.021.

[27] I. Ritucci, R. Kiebach, B. Talic, L. Han, P. Zielke, P.V. Hendriksen, H.L. Frandsen, Improving the interface adherence at sealings in solid oxide cell stacks, J. Mater. Res. 34 (2019) 1167–1178, https://doi.org/10.1557/jmr.2018.459.

[28] I. Ritucci, K. Agersted, P. Zielke, A.C. Wulff, P. Khajavi, F. Smeacetto, A.G. Sabato, R. Kiebach, A Ba-free sealing glass with a high coefficient of thermal expansion and excellent interface stability optimized for SOFC/SOEC stack applications, Int. J. Appl. Ceram. Technol. 15 (2018) 1011–1022, https://doi.org/10.1111/ijac.12853.

[29] A.W. Bredvei Skilbred, R. Haugsrud, The effect of dual atmosphere conditions on the corrosion of Sandvik Sanergy HT, Int. J. Hydrogen Energy 37 (2012) 8095–8101, https://doi.org/10.1016/j.ijhydene.2011.10.096.

[30] B. Talic, I. Ritucci, R. Kiebach, P.V. Hendriksen, H.L. Frandsen, Improved robustness and low area specific resistance with novel contact layers for the solid oxide cell air electrode, ECS Trans. 91 (2019) 2225–2232, https://doi.org/10.1149/09101.2225ecst.

[31] H.L. Frandsen, D.J. Curran, S. Rasmussen, P.V. Hendriksen, High throughput measurement of high temperature strength of ceramics in controlled atmosphere and its use on solid oxide fuel cell anode supports, J. Power Sources 258 (2014) 195–203, https://doi.org/10.1016/j.jpowsour.2014.02.036.

[32] H.L. Frandsen, P.V. Hendriksen, B.S. Johansen, A Testing Apparatus and a Method of Operating the Same, 2014. IPC No. G01N3/18; G01N3/20. (Patent No. WO2014195304.).

[33] I. Hofinger, M. Oechsner, H.-A. Bahr, M. V Swain, Modified four-point bending specimen for determining the interface fracture energy for thin, brittle layers, Int. J. Fract. 92 (1998) 213–220, https://doi.org/10.1023/A:1007530932726.

[34] KARA ferritic stainless steel chemical composition, (n.d.). https://www.aperam.com/sites/default/files/documents/FT_K36_en_web.pdf (accessed March 23, 2022).

[35] T. Manninen, J. Säynäjäkangas, Mechanical properties of ferritic stainless steels at elevated temperature, in: Proc. Fourth Int. Expert. Semin. Stainl, . Steel Struct., 2012.

[36] E. Kester, U. Rabe, L. Presmanes, P. Tailhades, W. Arnold, Measurement of Young's modulus of nanocrystalline ferrites with spinel structures by atomic force acoustic microscopy, J. Phys. Chem. Solid. 61 (2000) 1275–1284, https://doi.org/10.1016/S0022-3697(99)00412-6.

[37] C.-K. Lin, W.-H. Shiu, S.-H. Wu, C.-K. Liu, R.-Y. Lee, Interfacial fracture resistance of the joint of a solid oxide fuel cell glass–ceramic sealant with metallic interconnect, J. Power Sources 261 (2014) 227–237, https://doi.org/10.1016/j.jpowsour.2014.03.079.

[38] J. Malzbender, R.W. Steinbrech, L. Singheiser, Determination of the interfacial fracture energies of cathodes and glass ceramic sealants in a planar solid-oxide fuel cell design, J. Mater. Res. 18 (2003) 929–934, https://doi.org/10.1557/JMR.2003.0127.

[39] L. Zou, Y. Huang, C. Wang, The characterization and measurement of interfacial toughness for Si3N4/BN composites by the four-point bend test, J. Eur. Ceram. Soc. 24 (2004) 2861–2868, https://doi.org/10.1016/j.jeurceramsoc.2003.08.006.

[40] L. Zou, Y. Huang, C. an Wang, The characterization and measurement of interfacial toughness for Si3N4/BN composites by the four-point bend test, J. Eur. Ceram. Soc. 24 (2004) 2861–2868, https://doi.org/10.1016/j.jeurceramsoc.2003.08.006.

[41] L. Han, B. Talic, K. Kwok, P.V. Hendriksen, H.L. Frandsen, Interface fracture energy of contact layers in a solid oxide cell stack, ACS Appl. Energy Mater. (2020), https://doi.org/10.1021/acsaem.9b02026.

[42] I. Thaheem, D.W. Joh, T. Noh, K.T. Lee, Highly conductive and stable Mn1.35Co1.35Cu0.2Y0.1O4 spinel protective coating on commercial ferritic stainless steels for intermediate-temperature solid oxide fuel cell interconnect applications, Int. J. Hydrogen Energy 44 (2019) 4293–4303, https://doi.org/10.1016/j.ijhydene.2018.12.173.

[43] I. Thaheem, D.W. Joh, T. Noh, K.T. Lee, Highly conductive and stable Mn1.35Co1.35Cu0.2Y0.1O4 spinel protective coating on commercial ferritic stainless steels for intermediate-temperature solid oxide fuel cell interconnect applications, Int. J. Hydrogen Energy 44 (2019) 4293–4303, https://doi.org/10.1016/j.ijhydene.2018.12.173.

[44] C. Goebel, R. Berger, C. Bernuy-Lopez, J. Westlinder, J.E. Svensson, J. Froitzheim, Long-term (4 year) degradation behavior of coated stainless steel 441 used for solid oxide fuel cell interconnect applications, J. Power Sources 449 (2020) 227480, https://doi.org/10.1016/j.jpowsour.2019.227480.